Applied Thermal Engineering 243 (2024) 122587

Contents lists available at ScienceDirect

Applied Thermal Engineering

journal homepage: www.elsevier.com/locate/apthermeng

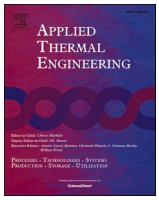

Research Paper

Power augmentation and Ramp-Up rate improvement through compressed air Injection: A dry low NOx combustor CFD analysis

Raditya Yudha Wiranegara, Uyioghosa Igie *, Artur Szymanski, Kamal Abudu, David Abbott, Bobby Sethi

Centre for Propulsion and Thermal Power Engineering, Cranfield University Cranfield, Bedfordshire, MK43 0AL, United Kingdom

ARTICLE INFO

Keywords:
Air Injection
Ramp-up rate
Power augmentation
Combustion
Emissions
Stability

ABSTRACT

Gas turbines play a key role in accelerating the transition towards more environmentally friendly power generation. This role includes backup of renewable generation that is intermittent, providing grid inertia as well as other ancillary services for grid stability. For quick backup power, the ramp-up rate of gas turbines can be improved through air injection at the back of the compressor, facilitated by integrating compressed air energy storage. Published works have mostly focused on low-fidelity engine system analysis of air injection overall effects. No study has focused on the detailed combustor performance presented in this study. The work shows the impact of air injection on the emissions, thermoacoustic stability and liner wall durability. These yardsticks in assessing the operability of the combustor have also been used for air power augmentation and ramp-up analysis. ANSYS software was used in the computational fluid dynamics (CFD) analysis of the three-dimensional dry low NOx combustor. Low-order models were used for the thermoacoustic stability and durability analysis. For the power augmentation study, the NO and CO emissions produced at 15 % air injection are below the maximum values of the combustor in design operations. Also, the stability and durability were within limits. The ramp-up investigation indicates up to 10 % air injection is allowed and the emissions are similarly acceptable. However, the thermoacoustic analysis shows a potential for combustion instabilities at high frequencies above 1800 Hz. Generally, there was no unusual wall liner durability in these two studies. When benchmarked against previous engine-level analysis, the ramp-up rate can be potentially improved by 54 % if the small concern on thermoacoustic instability is resolved.

1. Introduction

The proportion of renewable energy used in electric generation has been increasing. Despite being disrupted by the pandemic, the projected trend still shows a strong increase for the next 10 to 20 years [1]. With reducing the use of fossil fuel in the energy mix, the role of conventional electric generation, e.g., coal-fired and natural gas-fired power plants, will gradually shift from predominantly baseload (BL) to more as a backup for renewable power. The new role will require that these power plants no longer operate continuously over a sustained period, but rather for a few hours a day, during peak periods [2]. The intermittency of renewable generation and increased contributions present a challenge in maintaining electric grid stability. Gas turbines (GT) offer attractive ramp-up and load-following capability with lower CO and NO_x emissions than coal-fired power plants. The ramp-up rate of a GT is an important criterion for operational flexibility. To date, the average ramp-up rate of existing heavy-duty GT in open cycle configuration is approximately 9.6 % of BL output per minute [3]. Higher ramp-up rates will be required with an increase in the share of renewables introduced into the energy mix. Gonzales-Salazar et al. [3] predict that a ramp-up rate of up to 19.3 % of BL output per minute could be achieved.

GT original equipment manufacturers have been at the forefront of developing novel approaches to improving the ramp-up rate of engines. See Abudu et al. [4] which shows the ramp-up rate capabilities of different engines across major engine manufacturers. This information is presented in Fig. 1, which shows that currently, some of the highest ramp-up rate capabilities are dominated by the aero-derivative-type engines. This is due to the relatively smaller size and mass flows compared to the heavy-duty engines; in addition to the use of multiple spools that reduce the starting requirement in small to mid-sized engines. Nevertheless, heavy-duty GTs provide superior advantages for inertia and acting as a braking system for instability in the grid. A lot of research and development is continuously being done to improve the

* Corresponding author.
E-mail address: u.igie@cranfield.ac.uk (U. Igie).

https://doi.org/10.1016/j.applthermaleng.2024.122587
Received 21 September 2023; Received in revised form 10 January 2024; Accepted 29 January 2024
Available online 3 February 2024

Nomenclature

Abbreviations

CF	Correction Factor
GT	Gas Turbine
ST	Steam Turbine
PO-ISO	Power Augmentation at ISO ambient conditions
−5°C	Power Augmentation at −5 °C
+30 °C	Power Augmentation at 30 °C
ISO	International Standard Atmospheric
FAR	Fuel Air Ratio
FGM	Flamelet Generated Manifold
FTF	Flame Transfer Function
OEM	Original Equipment Manufacturer
MEL	Minimum Environmental Load
PDF	Probability Density Function
RKE	Realizable $k-\varepsilon$ model
RUR	Ramp-up Rate Improvement
CAES	Compressed Air Energy Storage
RANS	Reynolds-Averaged Navier Stokes
VIGV	Variable Inlet Guide Vane

Letters

c	Reaction progress
C_p	Heat capacity at constant pressure
C_μ	Turbulent viscosity constant
D	Effective diffusion coefficient
f	Mixture fraction
H	Enthalpy
k	Turbulence kinetic energy
l	Length scale
n	Gain
$P(v)$	PDF of variable v
q	Heat Release
S_c	Reaction Progress Source Term
t	Time
T	Temperature
u	Velocity
v	Fluctuation variable
x	Spatial direction
Y	Mass fraction of species

Greek Symbols

ε	Turbulence dissipation rate
ω	Angular Frequency
μ	Viscosity
ϕ	Equivalence ratio
ρ	Density
τ	Characteristic Time Delay
∇	Gradient

Letters and Symbols

$\widetilde{c^2}$	Reaction progress variance
$\widetilde{f^2}$	Mixture fraction variance
$\overline{\rho}\widetilde{u_i'u_j'}$	Reynolds stresses

Headings

$\sim$	Mean part from scalar decomposition/ Density-weighted averaged
$\mathring{A}$	Fluctuating part from scalar decomposition
$\cdot$	Non-weighted averaged
$\widehat{\ }$	Vector

Subscripts

i, j	Direction vector indexes
NO	NO (nitric oxide) species

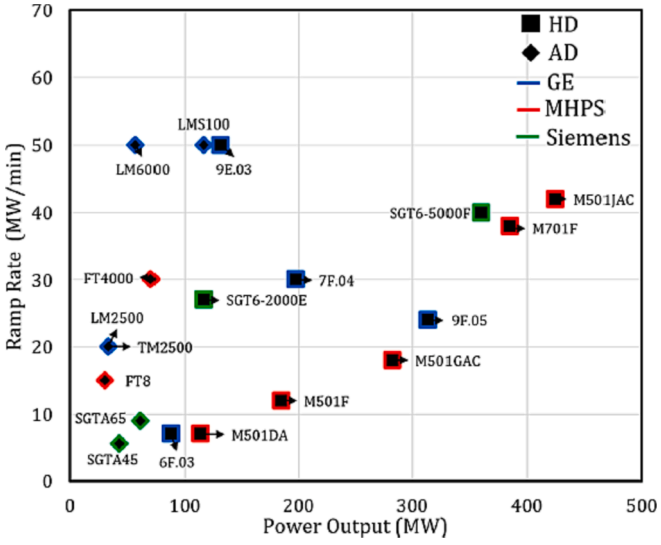

Fig. 1. Ramp-up rates of heavy-duty (HD) and aero-derivative (AD) gas turbines [4].

ramp-up rates of all GT configurations. However, it is clear why heavy-duty engines generally lag behind the aero-derivative machines.

An improved ramp-up rate irrespective of the fuel in use (natural gas, hydrogen or a blend of both) means that the engines can reach full or high-power outputs in shorter periods. This is to ensure that blackouts can be avoided if there is a sudden drop in renewable generation or a spike in energy demand. Some of the existing offerings for ramp-up include Siemens's improved operational procedure known as 'Start on the Fly' implemented in a combined cycle GT power plant [5]. The procedure enables the parallel start of both the steam turbine and GT by maintaining the temperature gradients at acceptable limits for all vital components. This is done by rapid repositioning of the variable inlet guide vane (VIGV) along with fuel control optimisation that ensures stable combustion during ramp-up. General Electric developed an approach called EGT^{TM} (electric GT) that includes an additional system in the form of battery storage [6]. It was featured with General Electric's aero-derivative GT. With a battery capacity of 10 MW and already high GT ramp-up capability for an aero-derivative, full power was reached in 10 min.

Other works have devised ways to improve the ramp-up rate by injecting compressed air into the GT. There are at least two approaches to air injection that can be found in the open literature. The first involves a modular package containing another set of combustion engines that drives an intercooled four-stage centrifugal compressor and a recuperator to heat the compressed air using recovered engine exhaust [7–9]. The compressed air then flows straight to the GT combustor. Through this approach, the engine could ramp up to full load in less than 60 s and an increase in power output of 10–20 % in a heavy-duty GT at standard atmospheric ambient conditions [10]. The second approach involves air injection into the GT with compressed air energy storage (CAES) operating at a greater pressure than the GT. The stored air is injected into the GT as a way of a fast start-up during peak period hence improving the

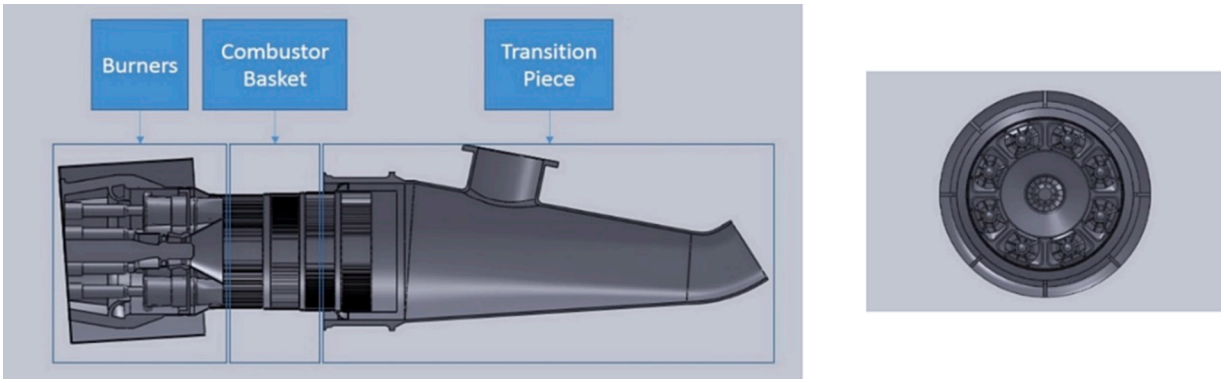

Fig. 2. 3D combustor model [19].

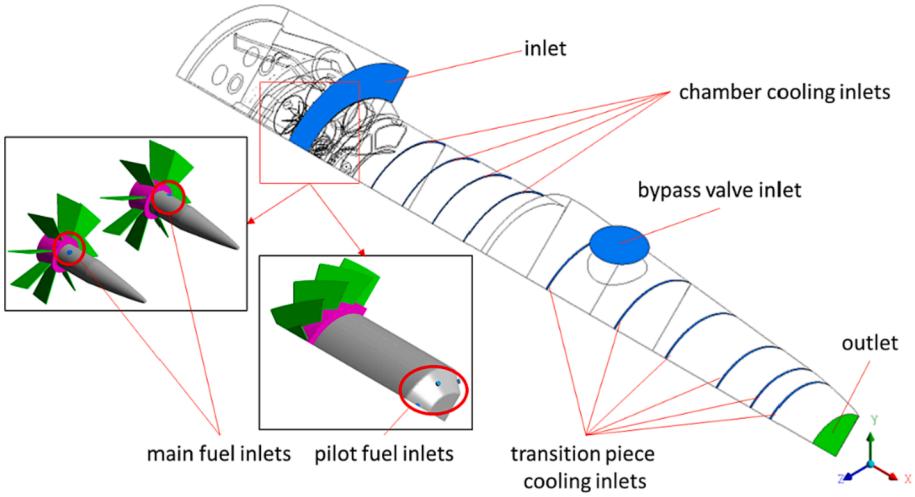

Fig. 3. Boundary definitions in the model [20].

ramp-up rate (transient operation). In addition, as a way of augmenting power in steady-state operation, addressed in the present study. The use of air injection has shown practicality in PowerPhase [11] where it was used for power augmentation for an aero-derivative engine.

Abudu et al. [12] investigated the heavy-duty engine-level analysis and performance with CAES air injection. The work shows a ramp-up rate improvement of 10 % for every 2 % increase in the compressed air injection at the back of the compressor. It also shows a power augmentation of 25 % which corresponds to a 15 % injection. Other GT-CAES-related works include Refs [2,13–17]. Most studies on the GT compressed air injection for ramp-up rate or power augmentation have focused on 0D engine-level performance benefits and more recently the authors also, show the aerodynamic effect on a standalone 3D CFD compressor [18].

No study in open literature investigated the impact of compressor air injection on the combustor provided in this present paper. We have proposed air injection as an alternative approach to improving the ramp-up rate of a gas turbine engine. For the first time, a holistic combustor performance investigation is presented using 3D RANS-CFD, indicating what impact air injection would have on the:

- emissions in terms of NO and CO, if these are significantly impacted compared to normal operations
- similarly, thermoacoustic stability, to check if unusual flame instability is triggered
- and combustor durability through the wall liner evaluation, to identify any potential excessive temperature rise that affects lifing.

As a result, the outcomes address the technical viability or operability of air injection (for ramp-up and power augmentation) in practical applications not previously studied.

To help produce realistic engine conditions, this investigation has taken advantage of the limit of air injection acceptable for the corresponding standalone high-fidelity 3D CFD compressor model [18]. A lot of their respective component boundary conditions have been informed by the overall engine-level analysis [12] published by the authors.

2. Methodology

This section consists of the methodology for modelling the 3D combustor, details about the model validation, as well as details of other supporting works of the authors leading to the present study.

2.1. Combustor model

The combustor model comprises three main parts, namely burners, a basket/chamber and a transition piece. The Mitsubishi-type DLN combustor houses a set of eight premixed main burners surrounding a single diffusion pilot burner placed at the centre of the arrangement in Fig. 2. Cooling is incorporated into the combustor chamber and the transition piece from the compressor. In the actual machine, a transition piece incorporates a bypass valve that acts as a load-varying mechanism during certain operating conditions.

Fig. 3 shows a quarter domain model along with its boundary conditions for the CFD simulation. A quarter domain has been considered for this work due to the significant computational requirement to

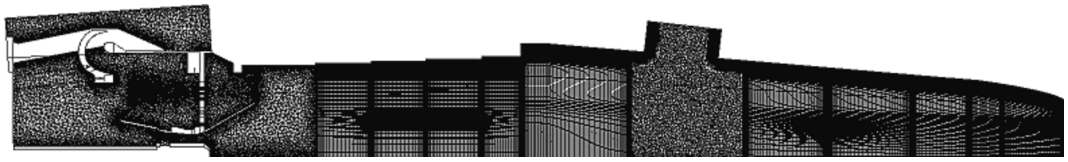

Fig. 4. Computational mesh of the quarter-model [19].

simulate the entire can. The boundaries of the domain consist of the combustor inlet, fuel inlets, cooling inlets (at the combustor chamber and transition piece), combustor outlet and solid walls. An inset is provided in the figure, to show an enlarged view of the main and pilot burners, also revealing the fuel inlets. Pressure and temperature are defined at the combustor inlet. Mass flow rate and temperature are defined at the combustor chamber and transition piece cooling inlets, with the temperature set to be similar to the inlet. The boundaries have been dictated by the recently published works of the authors [19] and [20] that are related to this study. As for the fuel used, it is pure methane (CH_4). The flow rate and the split between the main and pilot burners are scheduled in a similar manner against load. The chemical kinetics involved in the combustion of methane is described by the GRIMech 3.0 mechanism [21]. At the outlet, a target is set for the mass flow rate. With the target being specified, the pressure at the outlet is adjusted at every iteration until it meets the required mass flow rate. On the solid walls, a non-slip boundary is defined together with emissivity (0.7) and wall temperature (1000 K). Further details of the boundary conditions are indicated in **Section 2.3**.

2.1.1. Modelling – Turbulence, flame and emissions

A Reynolds-Averaged Navier-Stokes (RANS) model, realisable k - ε (RKE), is employed in this work. Two main governing equations of the model are shown in **Equation (1) and Equation (2).** It is a widely used model in most RANS combustion studies [22–26]. The term 'realisable' indicates its inherent capability to alleviate some mathematical constraints extended by the Reynolds stresses, enabling the model to be consistent with turbulent flow physics. Furthermore, Ref [27] point out that the viscosity constant, C_μ, is now a function of local mean flow deformation, instead of simply being a constant value, i.e., 0.09. Another distinctive feature of the model is its modified turbulent dissipation, ε^*, transport equation, derived from the fluctuating vorticity equation; hence, discarding the previously existing turbulent kinetic energy, k, production terms in the standard k – ε model.

k-equation:

$$\rho\frac{\partial k}{\partial t}+\frac{\partial}{\partial x_i}ku_j\rho=\frac{\partial}{\partial x_j}\left[\left(\mu+\frac{\mu_t}{\sigma_k}\right)\frac{\partial k}{\partial x_j}\right]+\mu_t S^2-\rho\varepsilon-2\rho\varepsilon M_t^2 \tag{1}$$

ε^*-equation:

$$\rho\frac{\partial \varepsilon^*}{\partial t}+\frac{\partial}{\partial x_i}\varepsilon^* u_j\rho=\frac{\partial}{\partial x_j}\left[\left(\mu+\frac{\mu_t}{\sigma_{\varepsilon^*}}\right)\frac{\partial \varepsilon^*}{\partial x_j}\right]+\rho C_1 S\varepsilon^*-1.9\rho\frac{\varepsilon^*}{k+\sqrt{\nu\varepsilon^*}} \tag{2}$$

where $\sigma_{\varepsilon^*}=1.2$, $C_1=\max\left[0.43,\frac{\eta}{\eta+5}\right]$, $\eta=S\frac{k}{\varepsilon^*}$, $S=\sqrt{2S_{ij}S_{ij}}$Accompanying the turbulence model is Flamelet Generated Manifold (FGM) [28], a partial-premixed combustion model, specifically employed for the combustion modelling in this study. The model assumes that a multi-dimensional turbulent flame consists of one-dimensional laminar flames in which all thermochemical properties are inherently embedded within each flame, forming a manifold or a database. The database is characterised by two scalar variables, namely mixture fraction (f) and reaction progress (c), and their variances, obtained from solving each variable's transport as seen in **Equation (3) and Equation (4)**.

$\widetilde{f}$-equation:

$$\frac{\partial\rho\widetilde{f}}{\partial t}+\frac{\partial}{\partial x_i}\left(\widetilde{f}\widetilde{u_j}\rho\right)=\frac{\partial}{\partial x_j}\left[\left(\frac{k}{C_p}+\frac{\mu_t}{\sigma_k}\right)\frac{\partial\widetilde{f}}{\partial x_j}\right], \tag{3}$$

$\widetilde{c}$-equation:

$$\frac{\partial\rho\widetilde{c}}{\partial t}+\frac{\partial}{\partial x_i}\left(\widetilde{c}\widetilde{u_j}\rho\right)=\frac{\partial}{\partial x_j}\left[\left(\frac{k}{C_p}+\frac{\mu_t}{Sc_t}\right)\frac{\partial\widetilde{c}}{\partial x_j}\right]+\rho S_c \tag{4}$$

where C_p is the heat capacity at constant pressure, Sc_t is the Schmidt number for turbulent flow and S_c is the source term for the reaction progress.

The fluctuating nature of turbulence combustion necessitates a function to describe the statistical distribution of these control variables. Hence, a joint Probability Density Function (PDF), $P(c,f)$ is acquired. The distribution shape of the joint PDF itself is assumed as β-function. A detailed description of the function is available in the authors' previous work [19]. In addition, a closure model is required for the reaction progress source term, S_c, (see **Equation (4)**. The term accounts for the physical-chemistry interaction between the turbulence and chemical reaction of the species involved, described by the wrinkling and thickening of the flame front by varying degrees of turbulence eddy scale. To account for this, a model developed by Zimont [29] is employed in this study. Similarly, the author's previous work has provided details of the equations and outlined the considerations that the model must cover.

NO being the major constituent of NOx emission, is considered in the calculation. Its calculation is decoupled from the turbulence-combustion modelling due to its relatively slower chemical timescale than the turbulent time scale. Hence, obtained as part of post-processing activities once convergence is achieved. A separate transport equation for the NO mass fraction (Y_{NO}) is acquired and can be expressed in **Equation (5)**.

$$\rho\frac{\partial\widetilde{Y_{NO}}}{\partial t}+\frac{\partial}{\partial x_i}\widetilde{Y_{NO}}\widetilde{u_j}\rho=\frac{\partial}{\partial x_j}\left[\rho D\frac{\partial\widetilde{Y_{NO}}}{\partial x_j}\right]+S_{NO} \tag{5}$$

where $\widetilde{Y_{NO}}$ is the mass fractions of NO and D is the effective diffusion coefficient. Each formation pathway constitutes a different definition of the NO reaction source term, S_{NO}. The authors' previous work includes the equation for the mean of the NO reaction source term, given that the turbulence effect influences the flame, thus the formation of NO. The formulation also considers the use of the joint PDF, which is assumed as β-function.

Lastly, the computational mesh used in this study is shown in Fig. 4. It is the same mesh employed by the authors in their previous work, Wiranegara et al. [19], which also presents the mesh independence study, together with the verification of the model when compared to the experimental study reported by Ruan et al. [30]. Having conducted a mesh independence study on three mesh cases (6.3, 10.6, and 23.1 million nodes), Wiranegara et al. [19] justify that the 10.6 million node case is sufficient and appropriate. Near the wall, a y + of 30 is employed as the RKE model employs a standard wall function to capture the near-wall physics, requiring the y + to be above 30 within the inner layer of the log-law region.

2.2. Thermoacoustic instability

There are different approaches for numerically predicting thermoacoustic instabilities. They include directly using time-varying Large

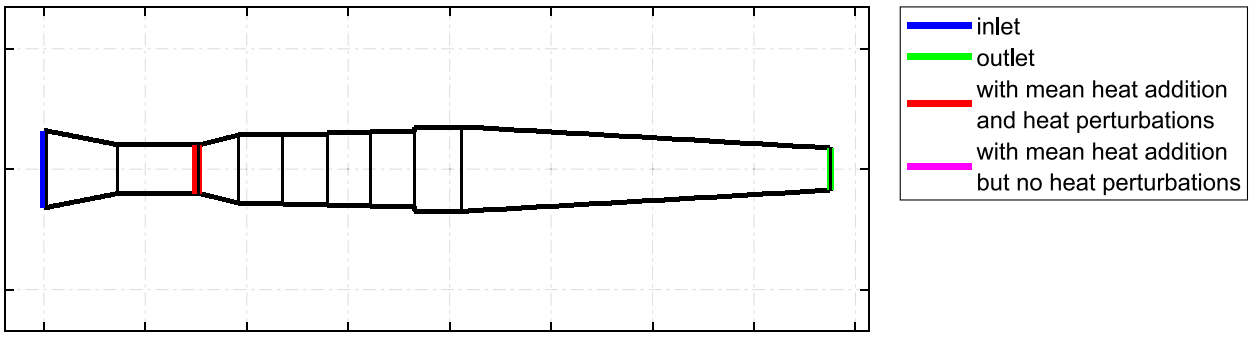

Fig. 5. Combustor geometry used in the analysis [20].

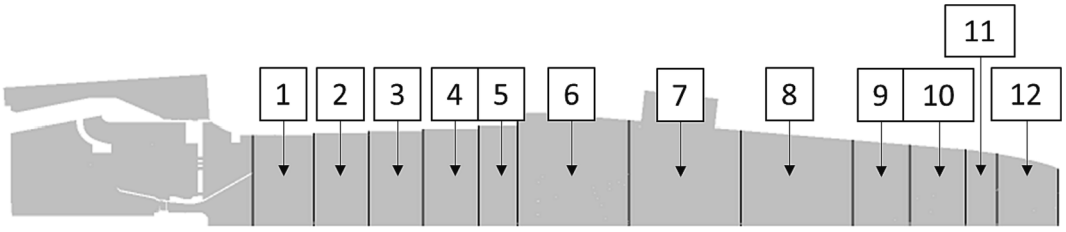

Fig. 6. Segments from the combustor model [20].

Eddy Simulation in which all appropriate geometry and acoustic boundary conditions and losses are included. In this case, acoustic oscillations are coupled with fluctuating heat release from the combustion flame and instabilities will grow or decay similarly to the real combustor. However, the approach is computationally demanding in terms of computer processor resources and often impractical for industrial-type studies [31]. An alternative approach is to decouple the calculations into a separate acoustic model together with a perturbed flame response [32]. The acoustic oscillation may be modelled using a low-order acoustic network model. For this approach, the fluctuating heat release due to the acoustic disturbances can be obtained from experiments, analytical or numerical simulations. The perturbed flame response can then be characterised either by a Flame Transfer Function (FTF) [33] for a linear analysis or a Flame Describing Function (FDF) [34] for a non-linear analysis.

Fig. 5 shows the simplified geometry used in the thermoacoustic analysis. The red line observed represents the source of the pilot and main flames. Calculations were conducted using an open-source code, OSCILOS which was developed by Professor A Morgans and her colleagues at Imperial College London [32]. The geometry has been simplified to fit the requirements of the code. In this work, the perturbed flame response was characterised by the FTF.

The FTF is expressed as,

$$FTF(\omega) = \frac{\hat{q}/\overline{q}}{\hat{u}_{ref}/\overline{u}_{ref}} \tag{6}$$

where ω is the angular frequency, $\hat{u}_{ref}$ and $\overline{u}_{ref}$ are the fluctuating velocity and mean velocity respectively at a location upstream of the flame, e.g., immediately upstream of the injection holes, $\hat{q}$ and $\overline{q}$ are fluctuating and mean heat release respectively. To obtain the FTF, either an experiment or time-dependent CFD simulation may be employed. However, these approaches are not always practicable. Hence, several models for simple FTF calculation have been proposed. One of them is the standard $n-\tau$ model [33]. The model is expressed as:

$$FTF(\omega) = ne^{-i\omega\tau} \tag{7}$$

here n is the gain that represents the magnitude of the interaction between acoustic oscillation and heat release fluctuation and τ is the characteristic time delay between inlet perturbation and the oscillation in heat release. In this work, the characteristic time delay is obtained through an approach inspired by the experimental work by Lieuwen et al. [35]. Acoustic oscillation is introduced upstream of the flame zone. The oscillation then propagates downstream towards the fuel injector inducing the equivalence ratio fluctuation. The unsteady mixture will finally reach the flame position, further inducing the heat release fluctuation. Hence, the time delay between the start time of equivalence ratio perturbation (due to the acoustic oscillation) and that of the heat release fluctuation is regarded as the characteristic time delay. In the context of simulation, this can be performed by virtually injecting tracking particles to travel from the fuel injection location to the flame position. The Discrete Phase Model (DPM) of ANSYS FLUENT was employed as the particle tracker method in this work. The flame position was marked by an *iso*-value of c 0.9 which is considered to represent the effective completion of combustion. Ruan et al. [36] describe the flame brush within the combustion primary zone as extending from c = 0.1 to c = 0.9. In practice, an interval of c between 0.89 and 0.91 was defined to provide an adequate layer of the flame boundary, to ensure all injected particles are captured by the surface.

2.3. Durability analysis

Combustion has a thermal impact on the liner wall's durability. In this section, the analysis focuses on the liner wall temperature distribution and the change, as a way of accounting for the impact of air injection. As peak temperatures exceeding the design limit have an impact on the combustor life, it is used here as an indicator of the impact of combustion on durability. Another Cranfield in-house 1D analytical code was used to perform the analysis. The code calculates the heat transfer between the hot gas and the liner wall using the Finite Difference Method (FDM) developed in MATLAB [37]. The code also considers the cooling geometry of a combined cooling system that incorporates impingement and effusion cooling methods. Several correlations are employed in the code to calculate the thermodynamic properties of the coolant. These are the specific heat capacity, heat conductivity and viscosity. The specific heat capacity is calculated using a curve-fitted polynomial expression provided in Ref [38].

The combustor liner wall considered in this code has a double-wall

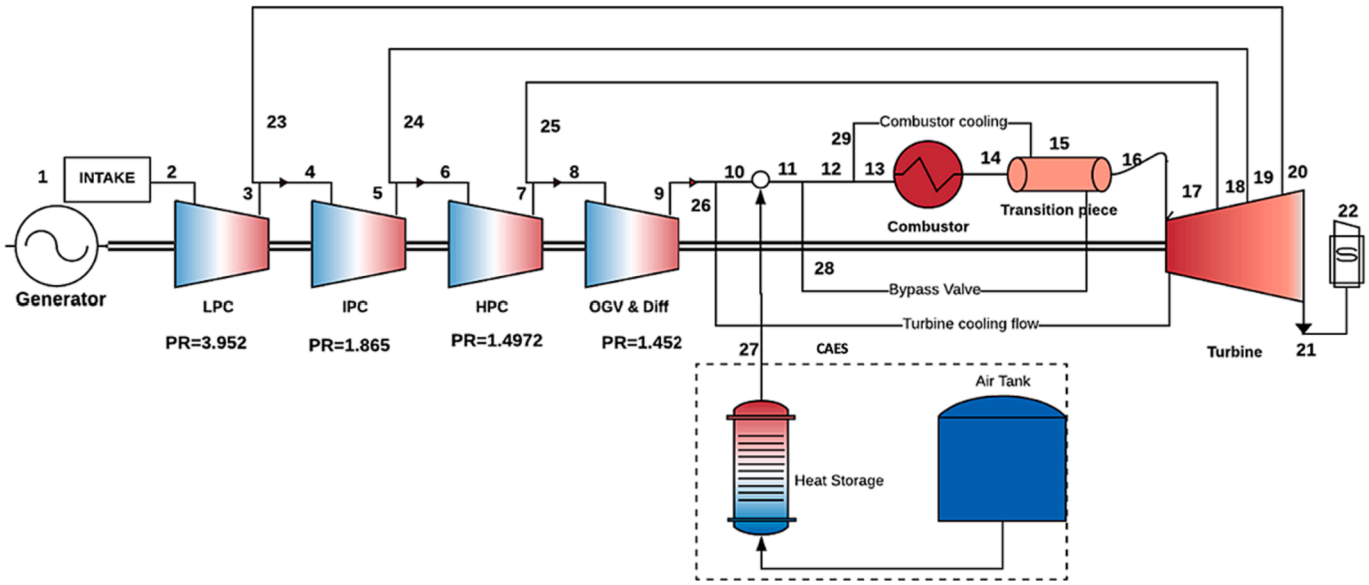

Fig. 7. Schematic of the engine model arrangement, indicating the location of CAES [12].

Table 1
Boundary conditions for design operations (ISO condition).

Parameters	Units	Baseload 100 %	Part-Load 83 %	Part-Load 68 %	Part-Load 47 %
Combustor inlet air pressure	Bar	15.9	14.1	12.2	11.2
Combustor inlet air temperature	K	692	667	654	683
Air inlet mass flow rate (quarter)	*kg/sec*	23.5	20.8	18.4	18.4
Bypass valve air inlet flow (% of air inlet)	%	0	4.51	8.7	14.2
Fuel	CH_4				
Inlet fuel temperature	K	413			
Global Equivalence ratio,ϕ	–	0.53	0.52	0.50	0.37
Pilot Equivalence ratio,ϕ_{pilot}	–	0.56	0.94	1.33	1.13

arrangement where the coolant flows within the enclosure of the walls. Hence, the domain of interest is located on the hot liner wall and is based on the heat balance equation. Using the FDM, the balance equation is then discretised at the domain of interest into nodal points and elements in the x and y directions. Before conducting the heat transfer analysis, the parameters required include the air mass flow rate distribution for the cooling and combustion, hot gas mass flow rate and cooling geometry. The bulk gas temperature for each segment was derived from the CFD simulations. Fig. 6 shows the twelve segments from the CFD model, which is based on the location of the cooling outlets shown in Fig. 3. For each segment, the information on the previously mentioned parameters was extracted. Parameters such as the air and hot gas mass flow rates were averaged at each axial plane generated across each segment. Hence, each segment is represented by a single value of each parameter, and these values were then input into the code. The calculation was individually performed for each segment resulting in the liner wall temperature for each segment shown in the later part of this paper.

2.4. Validation of CFD model and supporting studies

The authors of this study have previously validated their CFD model, as described in previous work [19]. In this paper, they compare the results of their CFD combustor with those obtained from a Mitsubishi experimental burner [39], under identical conditions. The comparison includes radial profiles of temperature and mass fractions of CO_2 at two axial planes relative to the burner inlet. Additionally, Ref [20] shows mass fractions of CO and NO in the *Appendix* of the referred study. The validation work indicates that the predictions between the CFD model and the experimental burner match better with an increased axial distance (plane B) away from the burner outlet. The maximum percentage errors for temperature and mass fractions of CO_2, CO, and NO at plane B (0.087 m from plane A) are 3 %, 13 %, 73 %, and 45 %, respectively. The mentioned studies within the TURBO-REFLEX project [40] have been supported by a validated Mitsubishi-type engine model developed by the authors in Ref [19] using an in-house gas turbine performance simulation code, TURBOMATCH [41]. This engine-level analysis shows the overall design and off-design (air injections) performance and was useful in providing the boundary conditions for the combustor CFD model here.

Fig. 7 is a schematic of the single-shaft engine model arrangement. The compressor sections were split only to devise a way to extract air for cooling other components of the engine. A dummy compressed air energy storage (CAES) is shown for illustration; the effects (temperature, pressure and flow) are accounted for, but not modelled. The injection into the engine is implemented between stations 10 and 11 as depicted in the figure. This figure also shows that boundary conditions such as combustor inlet pressure, temperature, airflow, fuel flow and bypass valve flows can be obtained for use in the CFD model. The fuel split ratio between the main and pilot and its scheduling against load were derived from a revised version of the schedule given by Tanaka et.al [39]. The boundary conditions are highlighted in

Table 1 which applies to the BL and part-load (PL) operations. Three PL operations are presented in this study and are: 83 % of the load, 68 % of the load (when the engine achieves its maximum variable inlet guide vane maximum closure) and 47 % of the load. That of 47 % is when the design minimum environmental load (MEL) is achieved [42]. Power augmentation has been conducted at BL at different ambient conditions. Their corresponding boundary conditions are presented in **Table A of the** *Appendix* and discussed subsequently.

The improved ramp-up rate scheduling obtained from the engine model [18] is shown in Fig. 8. This ramp-up rate (RUR) improvement is exhaustively explained in the referred work that employed the constant flow method and shows here that airflow injection is considered from

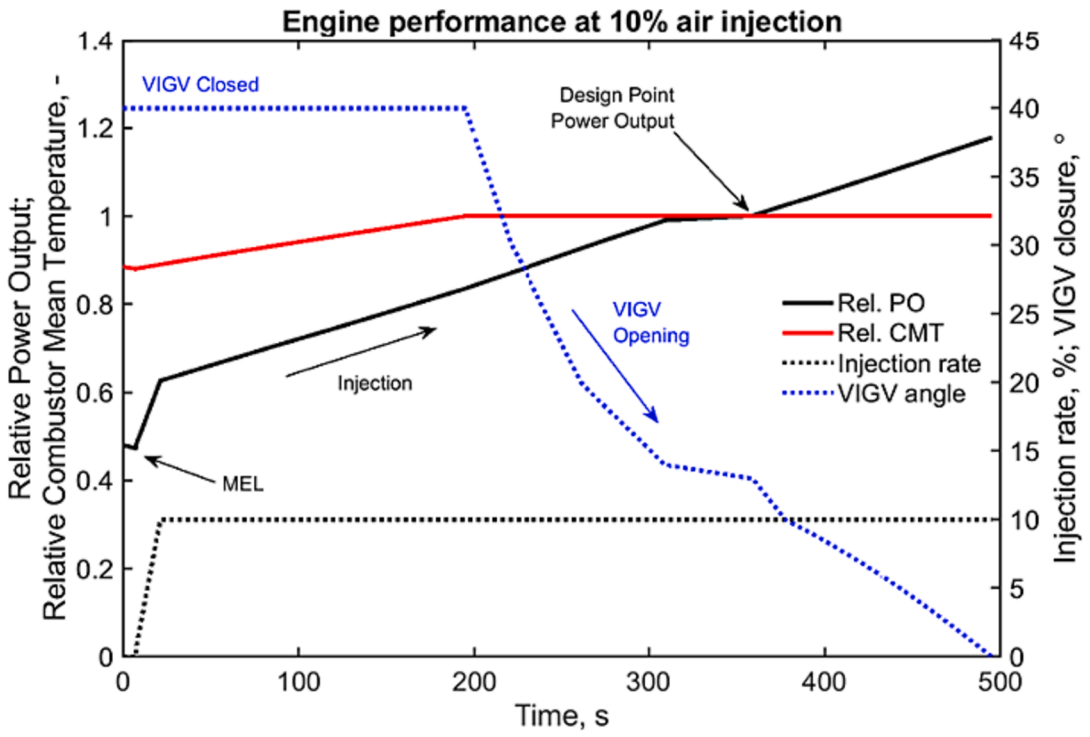

Fig. 8. Air injection ramp-up rate schedule [18].

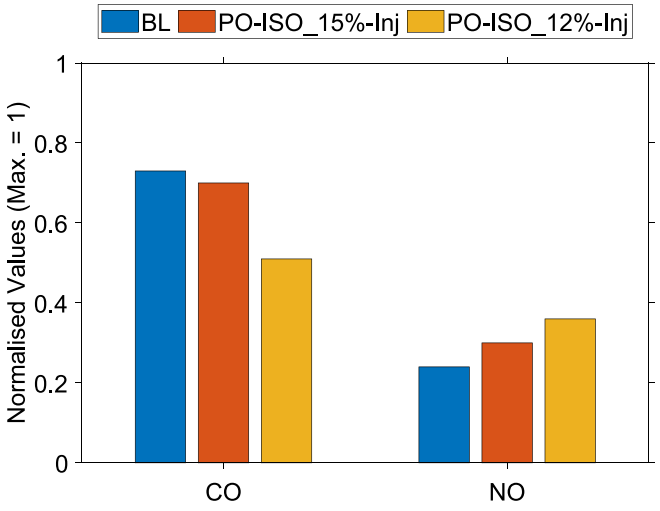

Fig. 9. Normalised CO and NO emissions at baseload and air injection cases at ISO.

MEL. It also shows that the maximum air injection is 10 % which was accompanied by a simultaneous increase in the opening of the VIGV. In this figure, CMT refers to the combustor mean temperature and PO is the power output in the engine model. The outcome of this quasi-transient study provides the background for the current study, indicating that the RUR can be improved by 10 % on average, for every 2 % (of compressor outlet) airflow injected irrespective of the starting load. It is important to note that for the air injection cases examined, the authors conducted a separate high-fidelity CFD analysis of the compressor [18] that shows that the 0D analytical engine model produced plausible results. Like the augmentation cases, the related boundary conditions for RUR are provided in the *Appendix* of this paper and discussed in the respective section.

3. Power augmentation

This section focuses on steady-state power augmentation at BL when the GT operates at 100 % output. It covers the international standard atmospheric (ISO) ambient conditions (ref ISO 3977) and other conditions (above and below the ISO temperature).

3.1. ISO conditions at baseload

The BL power output augmentation (PO) at ISO is presented here and denoted as PO-ISO. At BL, the bypass valve is fully closed and there is no bypass airflow into the transition piece. The fuel split ratio was initially set according to BL values. However, the ratio was found unsuitable for the air injection case, after preliminary work showed that the emissions, particularly the CO, infringed the limits set in Refs [19,20]. Hence, a new split ratio was considered for emission compliance. The ratio is relatively higher than the BL case as inferred from Table A1 **of the** *Appendix*. The corresponding engine level simulation [12] shows that for steady-state analysis, 15 % of air injection (based on compressor exit) at ISO will amount to a 25 % of power output increase. The robustness of the compressor to handle this without stall is shown in our high-fidelity compressor aerodynamic study [18]. Based on this finding, 15 % is the upper limit; additionally, we have included 12 % to expand the analysis here. Fig. 9 shows the CO and NO emissions at the outlet of the combustor, for BL condition and the two injection cases. It is important to mention that for the air injection cases, the air mass flow, pressures and temperatures into the combustor are greater than the BL (see Abudu et al [12] and **Table A**).

Fig. 9 also shows values that have been normalised with the highest value of each emission observed within the normal operating range. For this combustor design, the highest CO is found at part-load (PL) 47 % which is also MEL, while NO is at PL **68 %.** As a result, none of the values on the figure is up to 1. From the referred figure, it can be observed that none of these new operations infringe on the existing limit of the combustor. The higher NO emission in the injection cases is attributed to more fuel that has been injected into the pilot burners to control the CO emission, also reflected in the figure. **Table A** shows that the increase in

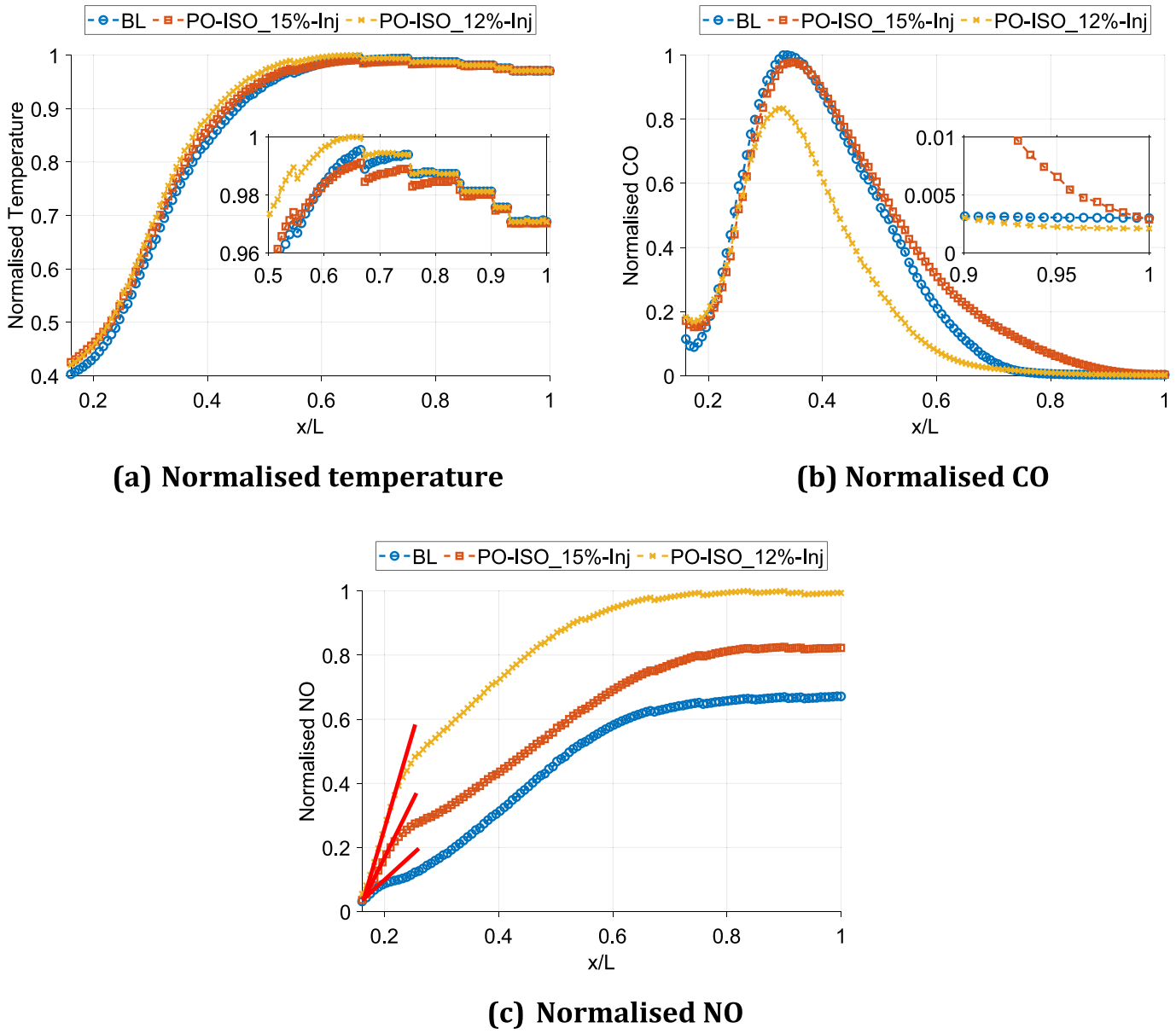

Fig. 10. Mass-average axial profiles of normalised parameters at baseload and injection cases at ISO.

fuel flow is mainly through the pilot burner which has a greater equivalence ratio. Axial and radial averaged profiles are provided subsequently, to enhance the understanding of the process that leads to the emissions outcome shown here.

Fig. 10 shows the axial averaged profiles of normalised temperature, CO and NO concentrations of all the cases considered in this section. The values have been normalised against the global maximum value of each parameter. The area of interest for the profiles has been limited to between the burner outlet of $x/L = 0.16$, and the combustor outlet, $x/L = 1$. From Fig. 10**(a)** it can be observed that the temperature profiles of the injection cases generally depict the characteristics expected from the BL. Below the relative axial distance of 0.5, all three cases show an increase in the temperature profiles at slightly different rates. The burner outlet shows that the BL starts at a temperature a few degrees lower than the injection cases, caused by a lower pilot equivalence ratio. The respective peak temperatures are shown and highlighted in the inset which shows clearer differences between these cases. From these, it can be observed that the 12 % injection case has the highest peak temperature, followed by the BL and the 15 % injection cases. The highest peak temperature for the 12 % case results from having the highest pilot equivalence ratio of the three cases.

From the CO concentration profiles in Fig. 10**(b)**, it can be observed that the 12 % injection case has consistently, the lowest values beyond $x/L = 0.2$. This is expected, due to having the peak temperature profile discussed, which will result in more CO burnout to CO_2. However, it is not entirely the case for 15 % injection, despite having a higher pilot equivalence ratio than the BL. This is attributed to the lower temperatures in the former particularly beyond $x/L = 0.5$. It is still important to mention that the CO levels at the combustor outlet are still marginally lower in the 15 % case, compared to the BL as shown in Fig. 10**(b)**. A detailed evaluation using the radially averaged profile is explained later. The NO concentration profile in Fig. 10**(c)** is as expected; the higher value in NO is due to a greater pilot equivalence ratio. The differences in NO across the combustor for the three cases are larger compared to the temperature and CO. Beyond $x/L = 0.8$ only a small increase is observed and attributed to the influence of the residence time at high temperatures.

The radial averaged profiles at five axial planes are presented in

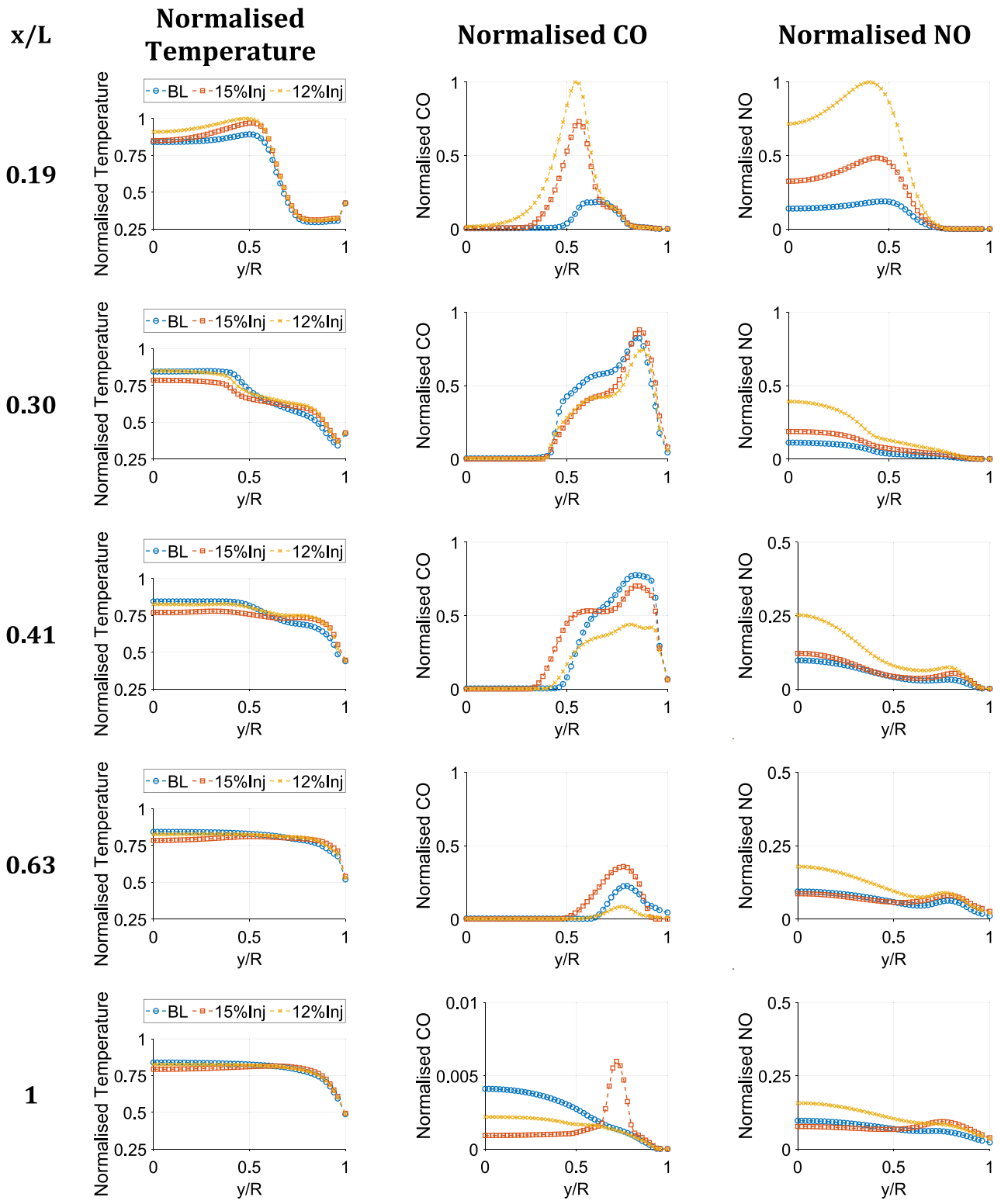

Fig. 11. Radial averaged normalised temperature, CO and NO concentrations for the baseload and injection cases at ISO across normalised axial locations.

Fig. 11. Like the previous figure, the same normalisation of temperature, CO and NO concentrations are used in Fig. 11; i.e., against the global maximum value of each parameter. It should be noted here that the range of the y-axis of some of the graphs varies to better highlight changes in operating conditions. From the normalised temperature profiles, the contribution of the main and pilot burners to the average temperature at respective axial locations can be better comprehended. Closer to the burner outlets at x/L = 0.19, the temperature is mainly influenced by the pilot burner. This is indicated by the region of high temperature that is located within the central region of the combustor y/R $\leq$ 0.5. This applies to all three cases, with the highest temperature peak seen for the 12 % injection case followed by the 15 % injection and BL case. It agrees with the averaged axial profiles in Fig. 10**(a)** at approximately the same axial location. The dominance of the pilot

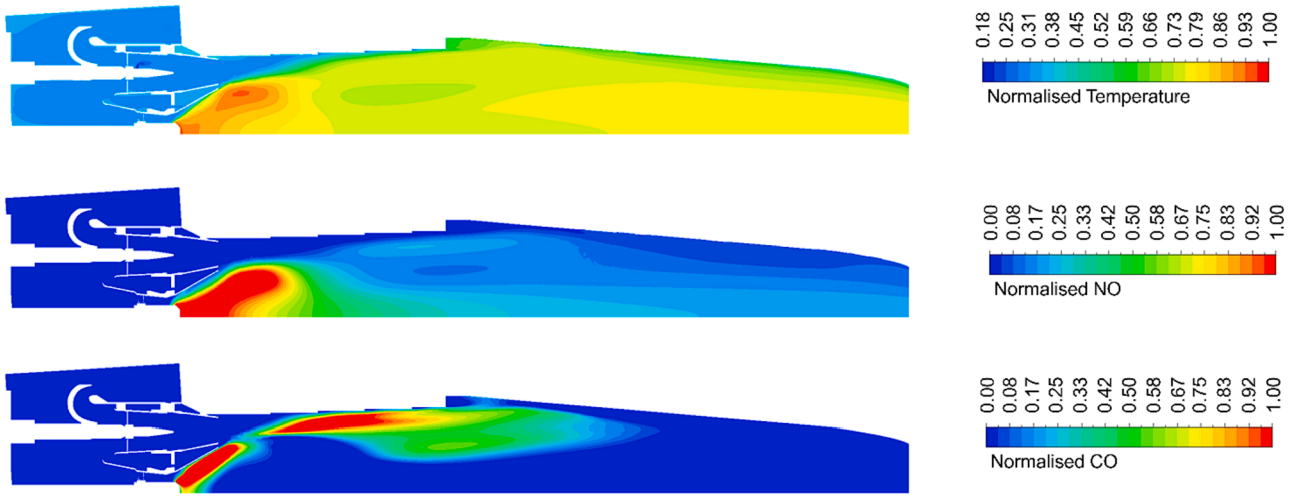

Fig. 12. Meridional contour plot of normalised temperature, NO and CO for 15% injection.

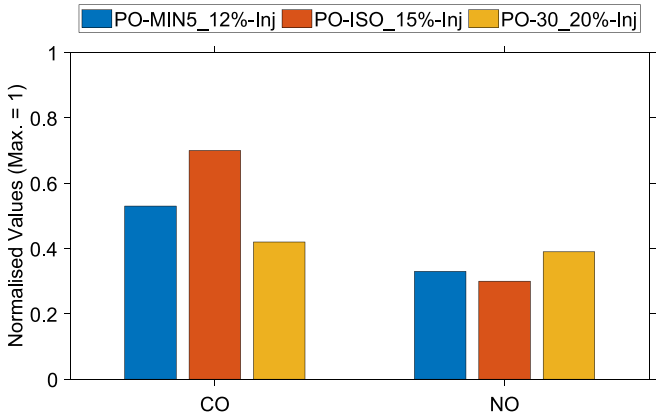

Fig. 13. Normalised CO and NO emissions with air injection at different flows and ambient temperatures: −5°C (PO-MIN5) and + 30 °C (PO-30).

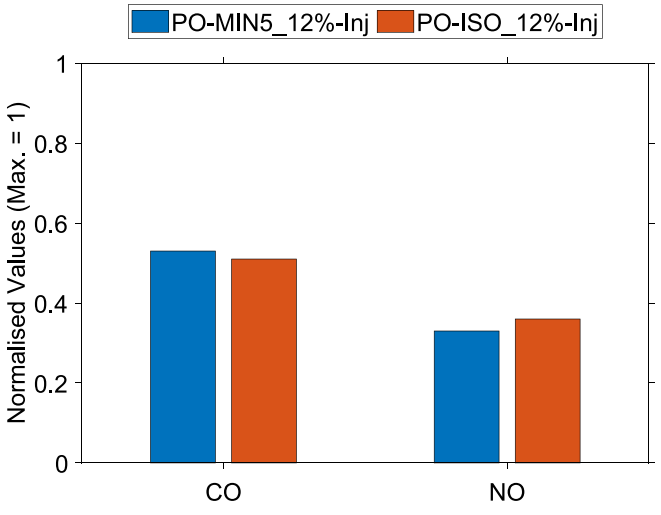

Fig. 14. Normalised CO and NO emissions with air injection at ambient temperatures −5°C (PO-MIN5) and ISO (both at 12 % injection).

burner is shown to reach $x/L = 0.41$, after which more contribution from the main burner is noticed and signified by the rise in the temperature above y/R = 0.5 across different axial locations towards the combustor outlet. At the outlet of the combustor where x/L = 1, it can be observed that radial temperature profiles have very few discrepancies. The corresponding CO profiles show more radial differences amongst the three cases across the combustor. Closer to the burner outlet, the highest CO concentration is observed to be between y/R ~ 0.5 and 0.8. This coincides with the region in which the highest temperature across radial positions is observed. Within the region, the chemical reaction is fast, as the timescale is dominated by turbulent mixing. At the combustor central region (i.e., for low y/R), the CO is seen to be very low, indicating complete combustion that could be attributed to the good mixing quality of the pilot burner. This is typically not the case relative to the main burner. However, the earlier work [19] of the authors shows that for this particular combustor design, the unmixedness in the pilot is relatively lower than the main burner. Further down the combustor axially (increasing x/L), it can be observed that the CO concentration increases between y/R ~ 0.5 and 1 that is combustor wall. This is caused by incomplete combustion in the mains burner mixture and is shown at locations for which there is complete combustion opposite of the pilot burner mixture. This behaviour and trends are dominant at x/L = 0.30, 0.41 and 0.63, until the combustor outlet x/L = 1, which shows a drastic change in the radial profile above y/R ~ 0.5. In the discussion on the axial averaged CO profiles of Fig. 10**(b),** the 15 % injection case was observed to have a lower burnout rate than the BL. Considering the CO radial profiles, the contribution of the lower burnout rate in the 15 % injection case can be attributed to the slow progress in the CO burnout of the main flame. At the combustor outlet, the view becomes clearer, particularly with the spike seen at the region above y/R = 0.5. The spike in CO concentration may result from the mixing quality of the main burner. As discussed in Ref [19], the fuel split shift from the main to the pilot may cause a reduction in the.

fuel jet momentum, hence impacting its ability to penetrate the freestream inside the burner and to be properly mixed. Therefore, the spike seen at the axial position at x/L = 1 could be a portion of incompletely burnt fuel being transported downstream. However, the combustor outlet value is still significantly below the target CO emissions value (i.e., the value seen at PL 47 % - MEL). Also, the average CO emission at the combustor outlet is still slightly lower than the BL shown in Fig. 9**.** The radial averaged profiles of the NO (Fig. 11) are mostly in line with their axial averaged profiles in Fig. 10**(c)**. The 12 % injection case is seen to have a high concentration of NO within the combustor central region, indicating the influence of the highest pilot equivalence ratio. As combustion progresses axially, the central region still contains the NO highest concentration in the 12 % injection case which continues to the combustor outlet. At $x/L = 0.41$ and beyond, the contribution of NO from the main burner mixture increases. These are highlighted in the

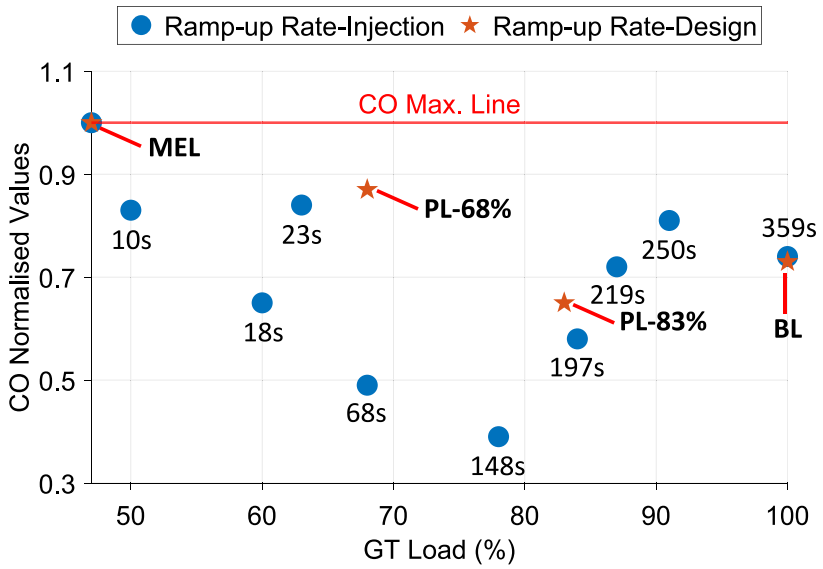

(a) Normalised CO emissions for discrete transient operations with other normal operations

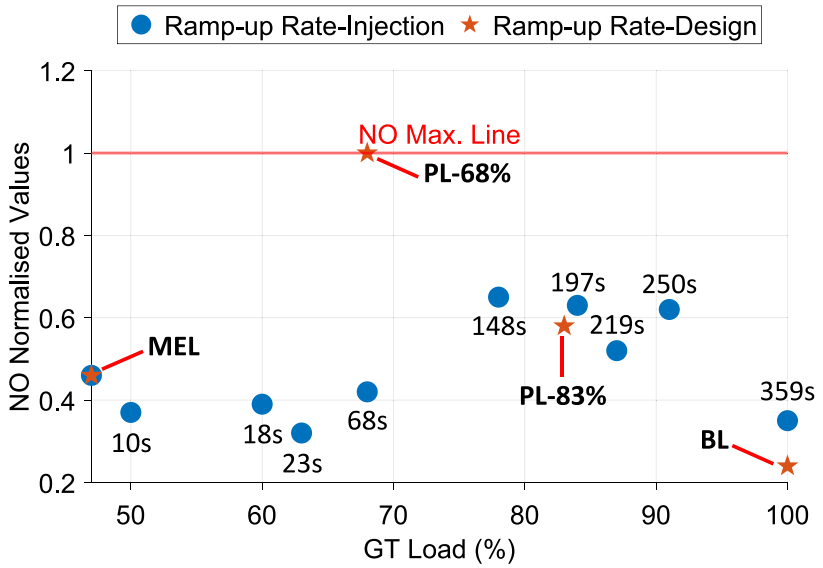

(b) Normalised NO emissions for discrete transient operations with other normal operations

Fig. 15. Normalised emissions with air injection for RUR improvement.

regions above $y/R = 0.5$. Despite this, the pilot burner is still a major contributor to the average NO emission at the combustor outlet, which is particularly so for the BL and 12 % injection cases.

In the 15 % injection case, the NO concentration of the pilot flame is concentrated around the pilot, at the end of the burner as indicated in Fig. 12. This also coincides with the area of peak normalised temperature in the figure. The contribution of NO from the main flame is significantly lower than that of the pilot and observed further downstream. On the other hand, the CO concentrations for both the pilot and main flames show high concentrations around their flames, nevertheless, are mostly burnt out by the exit of the combustor. Furthermore, the analysis shows that the injection cases for power augmentation at ISO conditions produce acceptable emissions. Despite higher NO emission than the BL case, the emissions, including the CO, are still far below the default limits or design peak values of the combustor that are referenced to PL 68 % for NO and PL 47 % for CO. The evaluation of the injection cases with respect to thermoacoustic performance and combustor liner wall durability is provided later in this paper, at the higher injection case of 15 %.

3.2. Lower and higher ambient temperatures at baseload

It is well known that low ambient temperature enhances the air mass flow and pressure into the combustor; the opposite is the case at a higher ambient temperature. The ambient temperatures considered are −5 °C and + 30 °C which have been simulated in the engine model [18]. At a constant combustor outlet temperature, the low ambient temperature results in a 22.5 % increase in the power output when supplemented with 12 % air injection. The high ambient temperature case allows for more air injection due to low air density and hence, 20 % air injection amounts to a 30.8 % increase in the power output. It is important to mention that these injection limits were determined by stall, in the corresponding detailed 3D compressor analysis by the authors [18]. Table A1 **of the** *Appendix* shows the boundary conditions, also with regards to the fuel split ratio. The PO-ISO fuel split ratio was initially adopted for these other conditions, however, produced unacceptable CO emissions for the + 30 °C case. This has been mitigated by increasing its pilot fuel ratio as shown, albeit having the lowest global equivalence ratio. Generally, in engine operation at constant combustion outlet

Table 2
Equivalence ratio and flame time delays of considered cases.

Case	GT Load [%]	φ_1 [-]	τ_1 [ms]	φ_2 [-]	τ_2 [ms]
Design Cases					
Baseload	100	0.034	2.687	0.516	5.603
83 % GT load	83	0.061	0.322	0.518	6.293
68 % GT load	68	0.081	0.192	0.485	7.316
MEL	47	0.068	1.227	0.382	8.458
Injection Case – Power Augmentation					
PO-ISO_15%-Inj	125	0.050	2.968	0.505	6.520
Injection Cases -RUR					
RUR-10s_2%-Inj	50	0.068	1.556	0.410	10.25
RUR-18s_8%-Inj	60	0.068	2.375	0.406	8.946
RUR-23s_10%-Inj	63	0.072	1.472	0.436	8.728
RUR-68s_10%-Inj	68	0.072	0.951	0.492	9.805
RUR-148s_10%-Inj	78	0.066	0.752	0.529	7.368
RUR-197s_10%-Inj	84	0.059	5.057	0.534	7.526
RUR-219s_10%-Inj	87	0.053	7.180	0.536	7.057
RUR-250s_10%-Inj	91	0.050	2.244	0.541	6.935
RUR-359s_10%-Inj	100	0.041	2.993	0.518	6.293

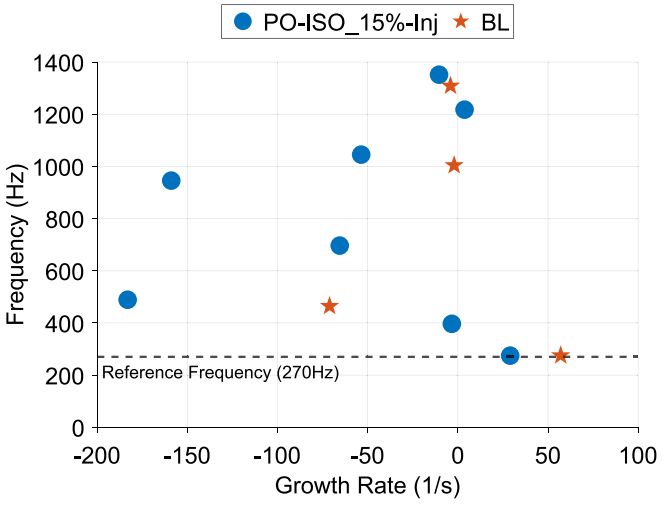

Fig. 16. Thermoacoustic instability frequencies and gains at baseload and 15% injection for power augmentation at ISO.

temperature, lower ambient temperature brings about an increase in fuel flow to maintain the referred temperatures. Air injection also has the same effect. For favourable conditions, the pilot equivalence ratio for the low ambient temperature is minimally above the ISO injection case. At higher ambient temperatures the air mass flows are lower and require less fuel flow to maintain the same combustor outlet temperature; however, the air injection has a counter effect. In this case, the highest pilot equivalence ratio is adopted.

Fig. 13 shows the normalised CO and NO emissions at BL ISO injection, as well as the lower and higher ambient temperature cases. The same normalisation and reference adopted in Fig. 9 are also used here. All three cases are observed to be below the emission limit as they are lower than one. The highest CO occurs at ISO conditions and is subsequently followed by −5 °C and + 30 °C. Nevertheless, at ISO conditions, the lowest NO emission is achieved. The strong influence of the pilot equivalence ratio in determining the emissions is reflected in the comparisons of the injection cases at different ambient conditions from Fig. 13. As explained, the equivalence ratio itself is defined by different operational parameters, including the fuel split ratio of each injection case which is greatly associated with the ambient condition. In the next comparison in Fig. 14, the cases being considered to have the same 12 % injection percentage and fuel split ratio. Therefore, the only difference between these cases is the ambient condition (-5°C and ISO). It can be observed that the effect of the ambient condition on the emissions is minor. At ISO, the CO emission is lower than at −5 °C. On the other hand, the NO is showing the opposite with the −5 °C case being the lowest.

4. Ramp-up rate improvement

The RUR improvement combustor analysis is presented here and related to the schedule shown in Fig. 8 for the quasi-transient engine simulation. This means taking several individual operating points along the ramp-up schedule and treating each point as a stand-alone steady-state case. The boundary conditions for each ramp-up instance (nine in total) are shown in Table B1 **of the** *Appendix*. Hence, the work assesses if the combustor can maintain acceptable emissions throughout the ramp-up, without exceeding the peak values of normal operations. Fig. 15 shows the CO and NO emissions for these nine simulation instances, presented as a function of the engine load. The figure indicates that none of these injection points exceeds the limits of normal design operations. In fact, Fig. 15**a** shows that for the same percentage of power output (68 %), the air injection case has significantly less CO which is about 44 %

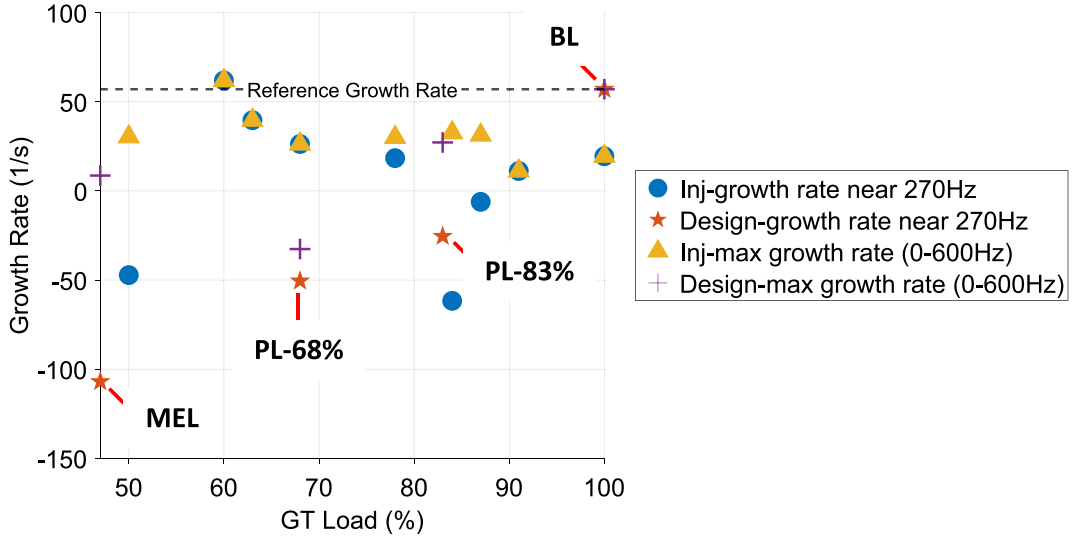

Fig. 17. Growth rates of the design operations and injection cases for RUR with the baseload growth rate line at reference frequency (~270 Hz).

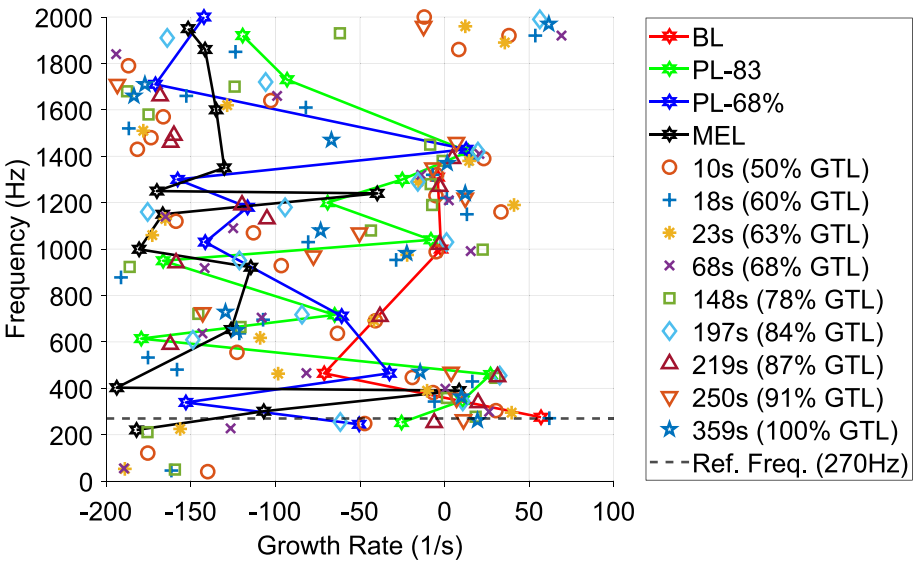

Fig. 18. Thermoacoustic instability analysis for RUR air injection cases.

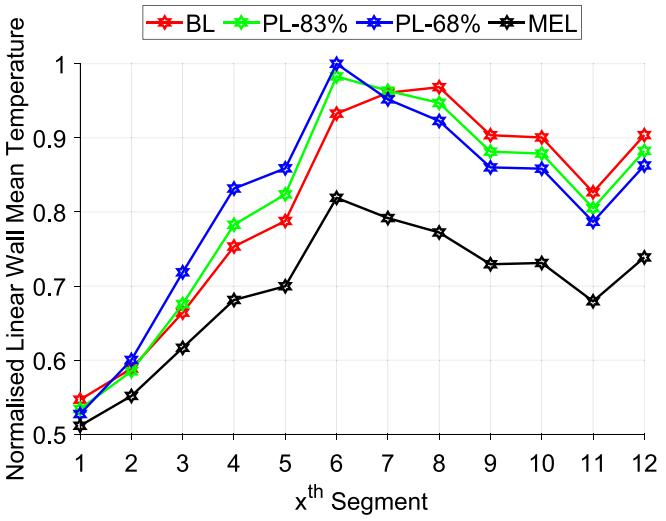

Fig. 19. Normalised liner wall mean temperature of each segment at different design operations.

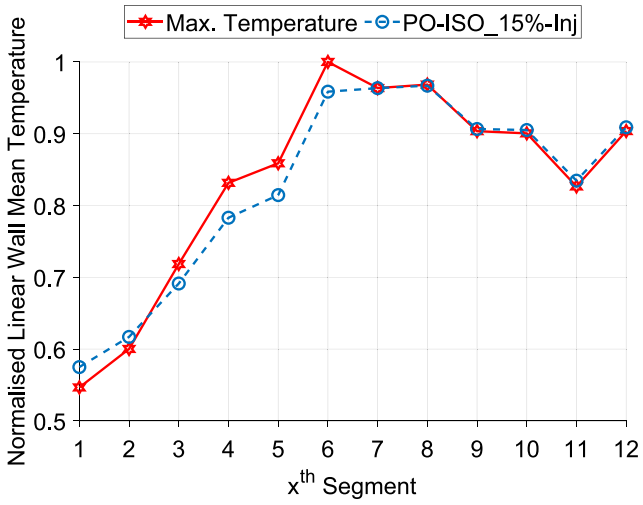

Fig. 20. Normalised liner wall mean temperature of each segment at peak design case temperature and 15% injection case for power augmentation.

less. Also, the NO is reduced by 58 %, as indicated in Fig. 15**b**. The performances of the injection cases for ramp-up rate improvement have been found to produce acceptable emissions. Part of the success can be attributed to the main/pilot fuel split schedule (**in** Fig. A1 **of the** *Appendix*) that was modified from the one used in the design cases, inspired by the schedule given in Ref [39].

5. Combustion stability

Thermoacoustic instability for normal operations and injection cases are presented here to evaluate the combustion stability. All design cases were considered for adequate comparison with the new air injection ramp-up cases. The purpose here is to identify if these new operations cause more instability in comparison to normal operations. Table 2 presents the equivalence ratio and flame time delays of the pilot and main burners. Subscript 1 represents the pilot flame zone and subscript 2 represents the main flame zone. The time delay was obtained using the technique described in **Section 2.2**. As observed from the table, the pilot flame region equivalence ratio, φ_1, is very small. This is due to the calculation of the ratio that includes fuel–air mixture inside the mixing tubes of the main burners. Therefore, reflect the correct overall temperature rise as indicated by the CFD simulation. Nonetheless, the local equivalence ratio is much higher than the overall value shown here. The information shown in the table in addition to the combustor inlet air flow boundary conditions and the combustor geometry (shown in Fig. 5) was used in the OSCILOS code to perform an eigenmode calculation for the system. The flame equivalence ratios along with the inlet pressure, temperature and velocity were employed to define the flame thermal properties. The flame time delays were used in conjunction with the linear $n-\tau$ model, for each flame. The inlet and outlet boundary condition have been defined as 'closed', as the combustor is situated between the compressor and turbine stages. The outcomes were the eigenfrequencies and their corresponding growth rates.

Fig. 16 includes the eigenfrequencies up to 1400 Hz for the comparison between baseload and 15 % injection for power augmentation at ISO cases. Frequencies with positive growth rates indicate a potential instability that could damage the combustor. A dash-line is added to the figure to indicate the 270 Hz frequency at which instabilities occurred in a similar combustor presented in Tanaka et al. [39]. Whilst the actual

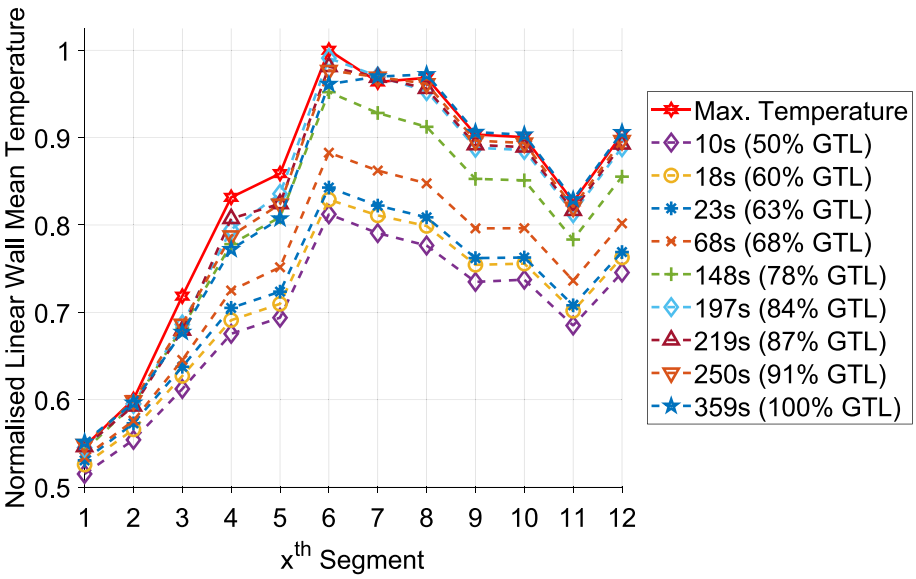

Fig. 21. Normalised liner wall mean temperature of each segment at peak design case temperature and RUR cases.

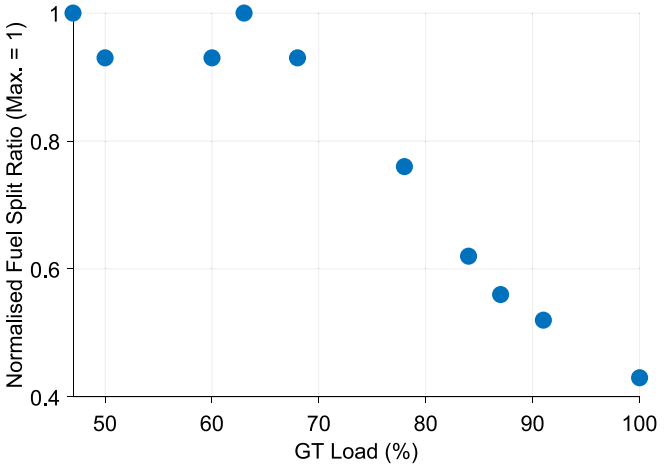

Fig. A1. Fuel split schedule for ramp-up rate improvement.

combustor mentioned incorporates dampers on the combustor transition piece to suppress instabilities, the present model did not include one. It is known that the use of dampers helps to mitigate combustion instabilities at BL. One predicted mode for the injection case observed at 270 Hz is presented with growth rates below the BL value of 57/s. Hence, it can be said for the particular mode, that the injection did not instigate further instabilities. Fig. 16 also shows that most of the eigenfrequencies from the PO-ISO_15%-Inj case are predicted to have a negative growth rate, except at the reference frequency where the growth rate is about 50% below the BL and thus considered acceptable. As the growth rate is a measure of which random fluctuation will grow, as the mode is excited, lower values than the BL indicate better stability, and hence there is no significant concern.

Due to the number of cases evaluated, a different presentation was used for the RUR improvement in Fig. 17. This figure includes other design or normal operations (BL, PL, MEL) for brevity and comparison, presented as a function of GT load. It is also referenced to the BL growth rate and frequency of 270 Hz. This approach is based on the finding in Ref [20] that has shown the BL has the highest growth rate of this frequency among other design cases. This figure shows that all the design operations have a growth rate below the BL and hence no concern for instability; this applies to other frequencies, as shown subsequently. Around the referenced frequency for air injection RUR, there exist modes of concern between 0 and 600 Hz.

Fig. 18 shows a comprehensive view of all the cases, plotted in frequency versus growth rate. At the reference frequency, most of the injection cases for RUR have lower growth rates. RUR-18s_8%-Inj, has a slightly higher value than the BL growth rate at the same frequency. Referring to the injection ramp-up schedule in Fig. 8, the case is located at the steepest slope of the relative power output line. This is when the injection rate is gradually increasing from 0 % to 10 %. Therefore, the instability at low frequency, as encountered here should not be a concern as it occurs during the transition towards the maximum injection at 10 % of air. High frequencies between 1800 and 2000 Hz show the main operations of concern. These are injection RUR cases (at 18 s, 68 s, 197 s and 359 s) with growth rates around or slightly above the

Table A1
Boundary conditions for air injection in simulating power augmentation at baseload different ambient temperatures.

Parameters	Units	Baseload	PO-ISO		PO (-5)	PO (−30)	PL-EFF
			Inj-15 %	Inj-12 %	Inj-12 %	Inj-20 %	Inj-10 %
Combustor inlet air pressure	Bar	15.9	18.2	17.8	19.9	17.9	13.5
Combustor inlet air temperature	K	692	725	717	704	754	682
Air inlet mass flow rate	*kg/sec*	23.5	26.8	26.2	28.9	25.9	20.2
Bypass valve air inlet flow (% of air inlet)	%	0					4.86
Fuel	–	CH_4					
Inlet fuel temperature	K	413					
Global Equivalence ratio,ϕ	–	0.53	0.52	0.52	0.53	0.50	0.51
Pilot Equivalence ratio,ϕ_{pilot}	–	0.56	0.77	0.78	0.79	0.82	1.30

Table B1
Boundary conditions for air injection in simulating ramp-up rate improvement.

Parameters	Units	RUR								
		10 s (Inj-2 %)	18 s (Inj-8 %)	23 s (Inj-10 %)	68 s (Inj-10 %)	148 s (Inj-10 %)	197 s (Inj-10 %)	219 s (Inj-10 %)	250 s (Inj-10 %)	359 s (Inj-10 %)
GT Load	%	50	60	63	68	78	84	87	91	100
Inlet air pressure	Bar	11.66	12.47	12.75	13.00	13.42	13.71	14.02	14.46	15.41
Inlet air temperature	K	640.61	655.56	661.26	666.85	676.29	682.44	684.73	687.76	694.29
Air inlet mass flow rate	kg/sec	18.72	19.81	20.17	20.17	20.16	20.20	20.61	21.17	22.38
Bypass valve air inlet flow (% of air inlet)	%	13.44	10.93	10.04	8.54	5.98	4.35	3.57	2.43	0
Fuel	–	CH_4								
Inlet fuel temperature	K	413.15								
Global Equivalence ratio,ϕ	–	0.38	0.39	0.39	0.42	0.48	0.51	0.52	0.52	0.53
Pilot Equivalence ratio,ϕ_{pilot}	–	1.06	1.06	1.12	1.12	1.03	0.91	0.82	0.77	0.64

referenced BL growth rate. They are of concern as they are high frequency and slightly higher growth rate operations. As indicated previously, given that dampers are not considered in this type of analysis, in practice this finding may be less pessimistic.

6. Durability - liner wall temperature analysis

The liner wall temperature analysis has been considered in evaluating the durability of the combustor when subjected to the new air injection operations. The purpose here is to investigate if the operating temperature significantly deviates from the normal design operations. Four design cases are considered, namely the BL and part-load (PL-83 %, PL-68 % and MEL). Fig. 19 shows the liner wall mean temperature distribution of the design cases that have been normalised against the maximum mean temperature of the 6th segment in the PL-68 % case. The distribution shows a gradual rise in temperature up to the 8th segment, which is followed by a subsequent decrease in the following segments. This is related to the location of the combustion peak temperature before the bypass valve with compressor air of lower temperature. Hence, in the latter segments, it can be observed that the temperature drops after the valve location.

Fig. 20 shows the comparison with the PO-ISO_15%-Inj case. As observed, the injection case is temporarily above the design cases in the first two segments, which is reflected from its axial averaged temperature profile in Fig. 10**(a)**. During the temperature rise between the 2nd and 6th segment, the injection case is shown to have a lower wall mean temperature than the design (maximum). Beyond these segments, they both have similar temperatures, which suggests that the PO-ISO_15%-Inj case would not pose any serious risk to the liner wall's durability.

Fig. 21 shows the temperature distribution for all the RUR injection cases. It indicates that the global peak temperature (normalised as 1) of the design operation that occurs at segment 6 is not exceeded. As a result, the ramp-up rate would not pose a serious risk to the combustor liner wall durability. However, locally at other segments, the 359s_RUR cases were observed to be marginally higher than the maximum temperature profile. This is at the 7th and 8th segments, by about 0.64 % and 0.40 % respectively.

7. Conclusions

The numerical work has focused on the impact that compressed air injection (for power augmentation and ramp-up rate improvement) will have on gas turbine engines. This is in the context of the combustor performance: emissions, combustor stability and durability that have not been previously investigated; yet are crucial factors in assessing the operability for practical applications. These cases have been supported with a corresponding analytical engine model from previous works of the authors that have been helpful with the provision of appropriate boundary conditions.

For power augmentation:

- a range of air injections during ISO has been tested. At 15 % injection, the CO emission was reduced by 4 % relative to the baseload. A larger CO drop of about 30 % was obtained for the 12 % injection. Nevertheless, their NO is greater than the baseload by 23 % and 48 % respectively. All these values notwithstanding are below the global maximum peak values of the design operations. This also applies to the injection cases at lower and higher ambient temperature operations investigated.
- The thermoacoustic instability analysis showed no risk during power augmentation. This is signified by eigenmodes with lower growth rates below that of the baseload.
- For the durability analysis (via the evaluation of the wall liner distribution), the maximum wall temperature is below the global maximum for the design operation. Hence no risk was posed in this new operation.

For ramp-up rate improvement:

- Nine sequential and discrete operating points across the ramp-up were selected for the study. The CO and NO emissions of these operating points are below the limit defined by the global maximum of design operations. In fact, for the identical power output of 78 % GT load, the injection case produced 35 % less NO than the normal operation for the same output. This is facilitated by the modification of the fuel split ratio in the injection case.
- For the thermoacoustic analysis, a small risk of combustion instability has been identified at high frequency operations of the injection cases. The instances of ramp-up rate operations have growth rates slightly higher than the maximum of the baseload case. Damper effects not accounted for in this study may bring about an optimistic interpretation of the actual risk to instabilities.
- The liner wall mean temperature distribution in these cases was found to be within and predominantly below local-segment temperatures. More importantly, below the global maximum peak temperature of the design operation. Hence no durability risk was posed.

This work has presented for the first time a high-fidelity operational viability study of a DLN combustor in handling high compressed air injection introduced at the back end of the compressor. The outcome has been promising for its potential to improve the operational flexibility of gas turbines with some cautious notes on the thermoacoustics. This type of analysis would benefit from more rapid ways of optimising the fuel split schedule and fuel split ratios, through the implementation of mathematical optimisation techniques to identify optimal operational set-up.

Research Data Management.

The author/s confirms that most of the data and methodology supporting the findings of this study are available within the article. Further data are not publicly available due to commercial and intellectual property rights.

CRediT authorship contribution statement

Raditya Yudha Wiranegara: Data curation, Formal analysis, Methodology, Investigation, Visualization, Validation, Writing – original draft, Writing – review & editing. **Uyioghosa Igie:** Conceptualization, Data curation, Formal analysis, Funding acquisition, Investigation, Methodology, Project administration, Resources, Supervision, Visualization, Writing – review & editing. **Artur Szymanski:** . **Kamal Abudu:** Formal analysis, Investigation, Methodology, Writing – review & editing. **David Abbott:** Conceptualization, Data curation, Formal analysis, Investigation, Methodology, Supervision, Writing – review & editing. **Bobby Sethi:** Conceptualization, Formal analysis, Investigation, Supervision.

Declaration of competing interest

The authors declare that they have no known competing financial interests or personal relationships that could have appeared to influence the work reported in this paper.

Data availability

The data that has been used is confidential.

Acknowledgements

This study is part of the TURBO-REFLEX project that has received funding from the European Union's Horizon 2020 research and innovation programme, under grant agreement No. 764545. We acknowledge the support of our industrial partner Mitsubishi Power, UK also involved in this study and work package.

Appendix

(See Fig. A1).
(See Table A1, Table B1).

References

[1] IEA, "World Energy Outlook 2020," Paris, 2020.
[2] U. Igie, M. Abbondanza, A. Szymański, and T. Nikolaidis, "Impact of compressed air energy storage demands on gas turbine performance," *Proceedings of the Institution of Mechanical Engineers, Part A: Journal of Power and Energy*, p. 095765092090627, Feb. 2020, doi: 10.1177/0957650920906273.
[3] M.A. Gonzalez-Salazar, T. Kirsten, L. Prchlik, Review of the operational flexibility and emissions of gas- and coal-fired power plants in a future with growing renewables, Renew. Sustain. Energy Rev. 82 (2018) 1497–1513, https://doi.org/10.1016/j.rser.2017.05.278.
[4] K. Abudu, U. Igie, I. Roumeliotis, A. Szymanski, G. Di Lorenzo, Aeroderivative gas turbine back-up capability with compressed air injection, Appl Therm Eng 180 (2020) 115844, https://doi.org/10.1016/j.applthermaleng.2020.115844.
[5] L. Balling, Fast cycling and rapid start-ups: new generation of plants achieves impressive results, *Modern Power Systems*, Jan. (2011).
[6] J. DiCampli, D. Laing, "State of the art hybrid solutions for energy storage and grid firming", POWER-GEN & Renewable Energy World, PGE 2017 Hybrid paper.pdf (accessed Feb, Europe 04 (2017) 2021), https://www.ge.com/content/dam/gepower-pgdp/global/en_US/documents/product/hybrid/GE.
[7] S. Arias Quintero S. Auerbach R. Kraft "performance improvement of gas turbine with compressed air injection for low density operational conditions", in volume 3a: coal, biomass and alternative fuels Cycle Innovations; Electric Power; Industrial and Cogeneration, American Society of Mechanical Engineers, Jun. 2014 10.1115/GT2014-27121.
[8] S. Quisenberry, L.L.C. PowerPHASE, Efficient Power Augmentation with Dry Air Injection, Industrial Application of Gas Turbines Committee, Alberta, Canada, 2015.
[9] P. Perri, A flexible generation and energy storage solution, accessed Feb. 05, 2021, Power Engineering (2017), https://www.power-eng.com/om/a-flexible-generation-and-energy-storage-solution/.
[10] P. Perri, "A Flexible Generation and Energy Storage Solution," *Power Engineering*, Nov. 15, 2017.
[11] B. Kraft, P. Perri, and S. A. Quintero, "Turbophase Dry Air Injection for Aeroderivative Combustion Turbines." Accessed: May 18, 2023. [Online]. Available: https://powerphase.com/white-papers/turbophase-dry-air-injection-for-aeroderivative-combustion-turbines/.
[12] K. Abudu, U. Igie, O. Minervino, and R. Hamilton, "Gas turbine efficiency and ramp rate improvement through compressed air injection," *Proceedings of the Institution of Mechanical Engineers, Part A: Journal of Power and Energy*, p. 095765092093208, Jun. 2020, doi: 10.1177/0957650920932083.
[13] R. Gay, M. Nakhmankin, S. Van der Linden, "Compressed air energy storage (CAES) with gas turbine air injection (AI) makes renewables and wind power more economic", in EESAT 2005 Conference, Sandia National Laboratories. (2005).
[14] N.M. Jubeh, Y.S.H. Najjar, Power augmentation with CAES (compressed air energy storage) by air injection or supercharging makes environment greener, Energy 38 (1) (2012) 228–235, https://doi.org/10.1016/j.energy.2011.12.010.
[15] J.D. Wojcik, J. Wang, Feasibility study of combined cycle gas turbine (CCGT) power plant integration with adiabatic compressed air energy storage (ACAES), Appl Energy 221 (2018) 477–489, https://doi.org/10.1016/j.apenergy.2018.03.089.
[16] M.J. Kim, T.S. Kim, Integration of compressed air energy storage and gas turbine to improve the ramp rate, Appl Energy. 247 (2019) 363–373, https://doi.org/10.1016/j.apenergy.2019.04.046.
[17] K. Abudu, U. Igie, I. Roumeliotis, A. Szymański, G. Di Lorenzo, Aeroderivative gas turbine back-up capability with compressed air injection, Appl Therm Eng 180 (2020) 115844, https://doi.org/10.1016/j.applthermaleng.2020.115844.
[18] A. Szymanski, U. Igie, R. Hamilton, Aerodynamic limits air injection for heavy-duty gas turbine: Compressor aerodynamic limits for power augmentation and ramp-up capabilities, Proceedings of the Institution of Mechanical Engineers, Part a: J. Power and Energy. 236 (7) (2022) 1257–1270, https://doi.org/10.1177/09576509221092510.
[19] R.Y. Wiranegara, U. Igie, P. Ghali, R. Zhao, D. Abbott, R. Hamilton, Numerical study of radiation and fuel-air unmixedness on the performance of a dry low NOx combustor, ASME Open J. Engineering 1 (2022), https://doi.org/10.1115/1.4055983.
[20] R.Y. Wiranegara, U. Igie, P. Ghali, K. Abudu, D. Abbott, R. Hamilton, Minimum environmental load extension through compressed air extraction: numerical analysis of a dry low NOx combustor, Appl Energy 336 (2023) 120803, https://doi.org/10.1016/j.apenergy.2023.120803.
[21] G. Smith *et al.*, "GRI-Mech 3.0." http://www.me.berkeley.edu/gri_mech/ (accessed Feb. 22, 2021).
[22] D. Jeong and K. Y. Huh, "Numerical Simulation of Non-Reacting and Reacting Flows in a 5MW Commercial Gas Turbine Combustor." 739–748 08 2009 10.1115/GT2009-59987.
[23] T. Cardoso de Souza, R. J. M. Bastiaans, B. J. Geurts, and L. P. H. De Goey, "LES and RANS of Premixed Combustion in a Gas-Turbine Like Combustor Using the Flamelet Generated Manifold Approach." pp. 1119–1127, Jun. 06, 2011. doi: 10.1115/GT2011-46355.
[24] J. S. Park, N. Yun, H. Moon, K. M. Kim, S.-H. Kang, and H. H. Cho, "Thermal Analysis of Cooling System in a Gas Turbine Transition Piece." pp. 1915–1924, Jun. 06, 2011. doi: 10.1115/GT2011-45961.
[25] Z. Mansouri, T. Boushaki, Experimental and numerical investigation of turbulent isothermal and reacting flows in a non-premixed swirl burner, Int J Heat Fluid Flow. 72 (2018) 200–213, https://doi.org/10.1016/j.ijheatfluidflow.2018.06.007.
[26] D. Pampaloni, P.C. Nassini, A. Andreini, B. Facchini, M. Cerutti, Numerical Investigations of Pollutant Emissions From Novel Heavy-Duty Gas Turbine Burners Operated With Natural Gas, J Eng Gas Turbine Power 142 (3) (2020), https://doi.org/10.1115/1.4045101.
[27] T.-H. Shih, W.W. Liou, A. Shabbir, Z. Yang, J. Zhu, A new k-∈ eddy viscosity model for high reynolds number turbulent flows, Comput Fluids 24 (3) (1995) 227–238, https://doi.org/10.1016/0045-7930(94)00032-T.
[28] N. Peters, "Laminar flamelet concepts in turbulent combustion," *Symposium (International) on Combustion*, 21 1 1231–1250 1988 10.1016/S0082-0784(88)80355-2.
[29] V.L. Zimont, Theory of turbulent combustion of a homogeneous fuel mixture at high reynolds numbers, Combust Explos Shock Waves 15 (3) (1979) 305–311, https://doi.org/10.1007/BF00785062.
[30] S. Ruan, N. Swaminathan, M. Isono, T. Saitoh, K. Saitoh, Simulation of Premixed Combustion with Varying Equivalence Ratio in Gas Turbine Combustor, J Propuls Power 31 (3) (2015) 861–871, https://doi.org/10.2514/1.B35517.
[31] Y. Xia, D. Laera, W.P. Jones, A.S. Morgans, Numerical prediction of the Flame Describing Function and thermoacoustic limit cycle for a pressurised gas turbine combustor, Combust. Sci. Technol. 191 (5–6) (2019) 979–1002, https://doi.org/10.1080/00102202.2019.1583221.
[32] J. Li D. Yang C. Luzzato A.S. Morgans Open Source Combustion Instability Low Order Simulator (OSCILOS-Long) Technical Report 2017 London UK.
[33] L. Crocco, Aspects of combustion stability in liquid propellant rocket motors part I: fundamentals. low frequency instability with monopropellants, Journal of the American Rocket Society 21 (6) (1951) 163–178, https://doi.org/10.2514/8.4393.
[34] A.P. Dowling, Nonlinear self-excited oscillations of a ducted flame, J Fluid Mech 346 (1997) 271–290, https://doi.org/10.1017/S0022112097006484.
[35] T. Lieuwen, H. Torres, C. Johnson, B.T. Zinn, A mechanism of combustion instability in lean premixed gas turbine combustors, J Eng Gas Turbine Power 123 (1) (2001) 182–189, https://doi.org/10.1115/1.1339002.
[36] S. Ruan, N. Swaminathan, M. Isono, T. Saitoh, K. Saitoh, Simulation of premixed combustion with varying equivalence ratio in gas turbine combustor, J Propuls Power 31 (3) (2015) 861–871, https://doi.org/10.2514/1.B35517.
[37] Y. Liu, et al., Development and application of a preliminary design methodology for modern low emissions aero combustors, 095765092091954, Proceedings of the Institution of Mechanical Engineers, Part a: J. Power and Energy (2020), https://doi.org/10.1177/0957650920919549.

[38] P.P. Walsh, P. Fletcher, Properties and Charts for Dry Air, Combustion Products and other Working Fluids, in: *Gas Turbine Performance*, in Wiley Online Books, Blackwell Science Ltd, Oxford, UK, 2004, pp. 102–142, https://doi.org/10.1002/9780470774533.ch3.
[39] K. Tanaka, K. Nishida, W. Akizuki, Gas turbine combustor technology contributing to environmental conservation, Mitsubishi Heavy Industries Technical Review 46 (2) (2009) 6–12.
[40] "TURBO-REFLEX." http://www.turbo-reflex.eu/ (accessed May 31, 2023).
[41] T. Nikolaidis TURBOMATCH Scheme for Aero/Industrial Gas Turbine Engine 2015 Cranfield University.
[42] K. Abudu, U. Igie, O. Minervino, R. Hamilton, Gas turbine minimum environmental load extension with compressed air extraction for storage, Appl Therm Eng 180 (2020) 115869, https://doi.org/10.1016/j.applthermaleng.2020.115869.

Power augmentation and Ramp-Up rate improvement through compressed air Injection: a dry low NOx combustor CFD analysis

Wiranegara, Raditya Yudha

2024-02-09

Wiranegara RY, Igie U, Szymanski A, et al., (2024) Power augmentation and Ramp-Up rate improvement through compressed air Injection: a dry low NOx combustor CFD analysis. Applied Thermal Engineering, Volume 243, 15 April 2024, Article number 122587

https://doi.org/10.1016/j.applthermaleng.2024.122587